PROGRESS IN COLOR, COLORANTS AND COATINGS

available online @ www.pccc.icrc.ac.ir

Progress in Color Colorants Coating 17 (2024), 239-262

Ministry of Science, Research and Technology
Institute for Color Science & Technology

Effect of the Coating Formulation on the Barrier Properties and Final Appearance of Non-wettable Hybrid Paper Sheets

G. Evren[1], Ç. Koşak Söz[1*], Z. Özomay[2], M. Uzun[3], S. Sönmez[2]

[1.] Faculty of Science, Material Science and Technologies, Turkish-German University, P.O. Box: 34820, Istanbul, Turkey

[2.] Faculty of Applied Technologies, Department of Printing Technologies, Marmara University, P.O. Box: 34722, Istanbul, Turkey

[3.] Faculty of Technology, Textile Engineering Department, Marmara University, P.O. Box: 34722, Istanbul, Turkey

ARTICLE INFO

Article history:
Received: 27 Oct 2023
Final Revised: 02 Jan 2024
Accepted: 07 Jan 2024
Available online: 17 Jan 2024

Keywords:
Cellulose
Coating
Paper
Packaging
Superhydrophobic

ABSTRACT

Thin coating layers of cross-linked polydimethylsiloxane (PDMS) and inorganic particles including glass spheres (GS), colloidal and fumed silica (aero and N20), montmorillonite (MMT), and kaolin (K) were attached onto Grade 1 Whatman filter paper (WFP) substrates using the spray-coating procedure to achieve superhydrophobic hybrid paper sheets. Coating formulations were varied in terms of their PDMS molecular masses and inorganic particles to prepare different samples. The effect of PDMS molecular weight and change in inorganic particle composition on the optical properties, surface roughness, barrier properties, surface chemistry, and topography was investigated. Hybrid paper sheets with ΔE_{00} values lower than 1 could be achieved, the surface roughness of which could be decreased by increasing the PDMS molecular weight in the coating formulation. Scanning electron microscopy studies revealed a homogeneous coating distribution, resulting in significant improvements in both the air and water barrier properties of the hybrid paper sheets. Spectroscopic investigations revealed the presence of interactions between the coating layer and the underlying paper substrate. Moreover, the distribution behavior of the inorganic particles on the spray-coated surfaces using the proposed method was also investigated using model compounds. Prog. Color Colorants Coat. 17 (2024), 239-262© Institute for Color Science and Technology.

1. Introduction

Academic interest in nonwettable paper (or cotton fabric)-based materials with superhydrophobic or hydrophobic surface properties has continued to grow in recent years [1-11]. Methods such as spray coating, dip coating, layer-by-layer coating, solution casting, physical vapor deposition, brush application, electro-fiber drawing method, chemical etching, and plasma treatment are generally used in the preparation of these materials, which are reported to have potential application areas such as oil/water separation systems, packaging materials, diagnostic and analysis devices, desalination membranes, gas sensors, liquid transport systems, or medical materials [6-9]. Among the many sophisticated characterization routes of paper-based superhydrophobic samples reported in the literature so far, spectroscopic interpretation of the surface chemistry, EDS-assisted scanning electron microscopy (SEM) studies for the investigation of the surface chemistry and topography, surface roughness measurements, and investigation of the optical and barrier properties of sample surfaces play an important role in revealing both

*Corresponding author: * soz@tau.edu.tr

https://doi.org/ 10.30509/pccc.2024.167221.1257

the basic science on which the study is based on and the possible application areas of the samples prepared [1-3, 5-7, 9-11].

In this study, we prepared nonwettable super-hydrophobic samples by coating a layer of cross-linked PDMS and inorganic particles onto WFP substrates. By designing our sample preparation procedure, we were inspired by the studies of Krumpfer and McCarthy about the modification of inorganic surfaces, with the help of which trimethylsilyl-terminated PDMS chains were attached on paper substrates. To explain the attachment of PDMS domains, either (i) the hydrolysis of PDMS followed by condensation with a surface silanol in the presence of a minor amount of water or (ii) the direct or acid-catalyzed silanolysis of PDMS by a surface silanol were hypothesized by Krumpfer and McCarthy, which are also suitable for modification of the organic paper surfaces because of their hydrophilic and slightly acidic nature. Moreover, samples were mainly characterized by the above-mentioned methods to understand the effect of the change in PDMS molecular weight and particle formulation in the coating layer on the optical, topographical, barrier, and chemical properties of our samples.

Nanocomposite coatings composed of a polymer matrix with inorganic particles in it is a highly relevant field of literature [12-15]. Studies on the preparation of superhydrophobic materials obtained by applying nanocomposite coatings onto the paper substrate surfaces are very common [6, 8-10]. Publications on samples coated with a PDMS-based nanocomposite layer are also present in this field [1, 3, 10, 11]. There are also various studies on the application of coatings composed of PDMS and inorganic particles onto paper substrates [16-20]. Ruan et al. coworkers, for example, applied a coating of PDMS and hydrophobic nanosilica particles onto polydopamine-coated tissue papers to design superhydrophobic surfaces with oil/water separation ability [16]. Zhang et al. applied a coating mixture of PDMS, epoxy resin, and nano-sized and micro-sized silica particles onto various substrates, including filter paper, by spray-coating. After curing the samples, the group achieved materials with superhydrophobic surfaces [20]. Teng et al. modified filter paper surfaces with a mixture of PDMS and PDMS-modified TiO_2 particles by the roll coating procedure to obtain nonwettable samples [17, 19]. In another study, Barthwal and coworkers applied superhydrophobic coatings of multi-walled carbon nanotubes, ZnO_2 particles, and PDMS onto various substrates, including filter paper, using the dip-coating procedure to prepare flame-retardant materials that also possess oil/water separation ability [18]. Ma and He sprayed mixtures of carbon nanotubes, PDMS, and foaming agent onto filter papers to prepare new superhydrophobic materials that behave like a conductive network [21]. Li et al. reported the application of a coating composed of epoxy resin, PDMS, nano-sized Fe_3O_4 and SiO_2 nanoparticles onto filter paper surfaces by spray-coating to get superhydrophobic and magnetic materials, which can also perform oil/water separation [22]. There are also publications on the preparation and characterization of superhydrophobic and paper-based samples containing trimethylsilyl-terminated PDMS in the coating formulation, but usually by the well-known hydro-silylation method in the presence of a catalyst [1, 3, 8, 10, 11]. So, there is no study on superhydrophobic and/or hydrophobic paper-based samples prepared with the method subject to our study.

This study can be regarded as a continuation of the previous studies on the hybrid paper sheets [23-26]. In our previous studies, we reported that the procedure selected for sample preparation is applicable for obtaining new packaging materials [14-16]. Here, the PDMS molecular mass in the coating formulation was varied to investigate its effect on the optical properties, surface roughness, barrier properties, surface chemistry, and topography of the hybrid paper sheets. Moreover, particle distribution behavior on the coating layers was investigated through model studies.

2. Experimental

2.1. Materials

WFP Grade 1 was purchased from General Electric (Turkey). Trimethylsiloxy-terminated PDMS with different molecular masses (PDMS-1.2K, PDMS-6K, PDMS-9K, PDMS-50K, and PDMS-92K) were purchased from Gelest (Morrisville, PA, USA). Aeroperl 300 Pharma colloidal silica (aero) was kindly supplied by Evonik (İstanbul, Turkey). GS, MMT, and K were purchased from Sigma Aldrich (Turkey). HDK N20 fumed silica, which is a synthetic and amorphous filler produced via flame hydrolysis, was kindly supplied by Wacker (İstanbul, Turkey) via IMCD Group (İstanbul, Turkey) [27, 28]. Reagent-grade tetrahydrofuran (THF) was purchased from Merck (Germany).

2.2. Preparation of the hybrid paper sheet samples

The sample preparation procedure was reported previously [16]. Briefly, a dilute PDMS solution was prepared in THF (0.7 wt. %) by magnetic stirring. Afterwards, inorganic particles were added to the PDMS solution. The ratio of each inorganic filler to PDMS was held at 1/1 in weight. Since each hybrid paper sheet had three types of inorganic filler in the coating formulation, the total weight of fillers to that of PDMS was in a 3/1 ratio. The mixture was stirred and sonicated and applied to WFP substrates via spray-coating. The samples were then left in the hood overnight and subjected to heat treatment at 120 °C for 36 h. Soxhlet extraction was performed with THF for 3 hours to get rid of the unreacted PDMS.

For the preparation of the control sample, a dilute PDMS solution was prepared in THF (0.7 wt. %) by magnetic stirring and sonication. The solution was applied to WFP substrates via spray-coating. The samples were then left in the hood overnight and subjected to heat treatment as described above.

2.3. Preparation of the model compounds

In order to investigate the distribution and agglomeration behavior of the particles on the surfaces with the proposed sample preparation and subsequent spray-coating method, model compounds were prepared and characterized via SEM and wide-angle X-ray spectroscopy (WAXD) [15, 16]. The solid weight percentage of the model compound mixtures was kept the same as the solid weight percentage of the superhydro-phobic coating formulations for ease of interpretation and comparison. The model compounds prepared for the SEM and WAXD studies are listed in Table 1.

Table 1: List of the model compounds prepared for the SEM and WAXD studies.

code	content abbreviation	solvent	weight percentage of the inorganic particle(s) in the solvent (%)
M-SEM-MMT	MMT	THF	0,7
M-SEM-K	K	THF	0,6
M-SEM-MMT/K/N20	MMT/K/N20	THF	0,2
M-WAXD-MMT-no treatment	MMT	-	-
M-WAXD-MMT	MMT	THF	0.7
M-WAXD-PDMS-6K/MMT	PDMS-6K/MMT	THF	0.7
M-WAXD-K-no treatment	-	-	-
M-WAXD-K	K	THF	0.6
M-WAXD-PDMS-1.2K/K	PDMS1.2K/K	THF	0.7
M-WAXD-PDMS-6K/K	PDMS-6K/K	THF	0.7
M-WAXD-PDMS-9K/K	PDMS-9K/K	THF	0.7
M-WAXD-PDMS-50K/K	PDMS-50K/K	THF	0.7
M-WAXD-PDMS-92K/K	PDMS-92K/K	THF	0.7

2.4. Characterization

Static and dynamic contact angle (CA) measurements were performed with a Dataphysics OCA 15 goniometer equipped with SCA 20_U software, as explained previously [14-16]. Bendtsen roughness values were determined using the L&W Bendtsen Tester. The average roughness (Ra) values of the samples in μm were obtained using a Zeiss ZEN Smartproof 5 confocal microscope and Zencore Smartproof software. Air permeance values were recorded with the help of the L&W Air Permeance Tester. Cobb tests were carried out. The CIE L*a*b* values of the paper substrates were measured with the Konica Minolta Spectrophotometer CM-700d [27]. The gloss values of the samples were measured using a BYK micro-gloss meter at 75º. Standards used in the characterization studies are given in Table 2. Attenuated total reflectance Fourier transform infrared (ATR-IR) spectra were taken with the help of a Perkin-Elmer FT-IR instrument, which is equipped with an ATR-IR spectrometer with a flat diamond plate. The spectra were collected with a resolution of 4 cm^{-1} and 32 scans were obtained for each spectrum [28]. SEM images were obtained on a high-resolution field emission environmental scanning microscopy (Thermo Fisher Quattro ESEM FE-SEM). The size of the imaged particles was measured using the ×T microscope server and Microscope Control (User Interface) software. EDS analyses were performed with the Pathfinder 2.8 software. X-ray diffraction studies were conducted on a Panalytical Emprean Diffractometer equipped with HighScore Plus (Malvern Panalytical) software.

3. Results and Discussion

In this study, 11 samples were subjected to characterization studies, as shown in Table 3. The WFP/PDMS-6K, which does not contain any filler particles in the coating formulation, was also investigated as a control sample. The thickness of the coating layer of the superhydrophobic hybrid paper sheets was determined according to simple gravimetric studies [16]: Coating thickness was found to be 5.8 ± 1.7 g/m^2, irrespective of the formulation of the coating layer, as given previously. The thickness of the WFP/PDMS-6K control sample was calculated to be 0.3±0.1 g/m^2, a value much smaller than that of the hybrid paper sheets, as expected.

Static and dynamic CA measurements were performed to understand the wetting behavior of the sample surfaces. As reported in the previous study, untreated WFP is inherently hydrophilic and has CA values around 0°. WFP/PDMS-6K samples also revealed hydrophilic behavior and absorb water droplets within seconds, although being coated with hydrophobic PDMS: PDMS coating is not sufficient to cover and hydrophobicize the whole porous surface of WFP. The PDMS layer does not fill completely all the voids of the fibrous paper substrate, as shown in Figure 9, so that water droplets could still be adsorbed by the paper substrate through the capillary effect [16]. For the dynamic CA measurements, performed to calculate the contact angle hysteresis values (CAH), the embedding needle method was selected. Accordingly, all the hybrid paper sheet samples (with numbers 2 to 11), reveal superhydrophobic behavior with water contact angle values above 150° and water CAH values below 10° [29], as being summarized in Table 3.

Based on the previous studies on hybrid paper sheets with varying PDMS masses in the coating formulation, we also have an idea about the mechanical properties of our samples [16]: Briefly, in the WFP/PDMS/GS/aero/N20 samples, coating application enhanced the wet tensile indices, as expected. The coated paper sheet having PDMS-6K in the coating formulation resulted in the highest relative wet strength

Table 2: Standards used in the characterisation studies.

Characterization study	Standard used
Bendsten roughness determination	Tappi T 479 om-91
Air permeance determination	Tappi T 460 om-88
Cobb test	Tappi T 441
Determination of the CIE L*a*b* values	ISO2470-2
Gloss measurements	ASTM D523

Table 3: Samples, which were prepared and characterized within the scope of this study.

#	sample code	CA (°)	CAH (°)
1	WFP/PDMS-6K (control)	0	-
2	WFP/PDMS-1.2K/GS/aero/N20	159.0 ± 1.8	7.2 ± 1.3
3	WFP/PDMS-6K/GS/aero/N20	161.9 ± 1.5	5.4 ± 1.0
4	WFP/PDMS-9K/GS/aero/N20	160.2 ± 1.1	6.8 ± 1.9
5	WFP/PDMS-50K/GS/aero/N20	161.1 ± 2.0	6.2 ± 1.4
6	WFP/PDMS-92K/GS/aero/N20	160.4 ± 1.2	7.1 ± 1.1
7	WFP/PDMS-1.2K/MMT/K/N20	162.0 ± 1.1	5.1 ± 1.7
8	WFP/PDMS-6K/MMT/K/N20	163.4 ± 2.0	3.4 ± 0.7
9	WFP/PDMS-9K/MMT/K/N20	161.8 ± 0.7	6.1 ± 1.8
10	WFP/PDMS-50K/MMT/K/N20	161.5 ± 0.3	6.9 ± 1.1
11	WFP/PDMS-92K/MMT/K/N20	161.7 ± 0.6	7.4 ± 1.3

values in both directions, with values of 2.49 ± 0.35 Nm/g in MD and 1.97 ± 0.49 Nm/g in CD, respectively. These values were measured to be 2.25 ± 0.59 Nm/g and 1.73 ± 0.37 Nm/g for WFP. The WFP/PDMS/MMT/K/N20 samples have significant increases in wet tensile index values reaching up to 4.9 Nm/g in MD and 3.9 Nm/g in CD, which are much higher than those of the WFP/PDMS/GS/aero/N20 samples, revealing the positive effect of the platelet-shaped particles in the coating formulation. However, no effect of PDMS molecular weight on the mechanical properties was detected. Moreover, the relative wet strength values of WFP were calculated to be 3.7 and 3.4 % in MD and CD, respectively. For the WFP/PDMS/GS/aero/N20 samples, the highest increase was detected for the hybrid paper sheet having PDMS-6K in the coating formulation, with 10.5 % (MD) and 9.8 % (CD) in relative wet strength values. The increases in relative wet strength values were much more pronounced and were up to 20 % in both directions for the samples having the formulation WFP/PDMS/MMT/K/N20.

In this study, Whatman Grade 1 filter paper was preferred due to its high cellulose content (96 %) [30]. The presence of -COOH groups of hemicellulose on the paper surface is predicted to be negligible, which was also demonstrated by preliminary FT-IR studies published before [15]: No C=O peak of carboxyl groups is observed at 1600 cm^{-1} for Whatman Grade 1 filter papers [31]. Moreover, it is known that the paper surface and materials derived from cellulose in general (nanocellulose particles, etc.) are hydrophilic and slightly acidic in nature [32-37]. In light of these informations, it is known that -OH and -O- functional groups dominate the Whatman Grade 1 paper surface. Within the scope of our study, a PDMS/inorganic particle mixture was prepared in tetrahydrofuran (THF) solvent, and the dispersion was applied to paper surfaces by spray-coating [34, 38, 39]. After the THF solvent was evaporated, samples were subjected to heat treatment to fix the coating on the paper surface. It is known that the presence of THF instead of water as a solvent affects the surface charges, pH of the environment, and swelling behavior of paper. However, since the THF evaporates before heat treatment, it is thought that THF has no effect on the interactions between the coating and the paper substrate.

3.1. Optical properties

3.1.1. The color difference (ΔE_{00})

The ΔE_{00} value indicates the color difference between the displayed color and the original color of the samples. A low ΔE_{00} value indicates that both colors are very close to each other, while a very high ΔE_{00} value indicates a difference between those [40]. In the $\Delta E_{00} \leq 1$ case, the color difference cannot be perceived by the human eye. If the ΔE_{00} value is between 1 and 2, the color difference can only be detected by

examination with a measuring device. ΔE_{00} values between 2 and 3 indicate color differences, which cannot be easily perceived by most observers. A ΔE_{00} difference of 3 or higher, on the other hand, indicates that the color difference can be easily recognized by the human eye [41-43]. The color difference (ΔE_{00}) of the coated samples compared to the uncoated control sample was calculated (Eq. 1).

$$\Delta E_{00} = \sqrt{\left(\frac{\Delta L'}{KLSL}\right)^2 + \left(\frac{\Delta C'}{KcSc}\right)^2 + \left(\frac{\Delta H'}{KHSH}\right)^2 + RT\left(\frac{\Delta C'}{KcSc}\right)\left(\frac{\Delta H'}{KHSH}\right)} \quad (1)$$

where: RT is the hue rotation term; KL, KC, and KH are the parametric factors for variation in the experimental conditions; S is the compensation for lightness; SC is the compensation for Chroma; SH is the compensation for Hue; ΔL'is the transformed lightness difference; ΔC'is the transformed chroma difference and ΔH' is the transformed hue according to the ISO13655-18 testing standard.

Table 4 shows the CIE L*a*b*-color values of the control and the coated samples. According to the obtained values for the PDMS/GS/aero/N20 samples (for samples having only spherical inorganic particles in the coating), there is a trend towards lower ΔE00 values with increasing PDMS molecular weight in the coating formulation. Since $\Delta E_{00} \leq 1$ except WFP/PDMS-1.2K/GS/aero/N20, it can be said that the color difference that cannot be perceived by the human eye for the PDMS/GS/aero/N20 samples. For the PDMS/MMT/K/N20 samples, on the other hand, there was an increase in a* values (red nuance was increased), with increasing PDMS molecular weight in the coating formulation. Moreover, there is also a trend towards negative b* values, which means that the blue nuance was increased with increasing PDMS molecular weight. Increasing the PDMS molecular weight in the coating formulation also increased the ΔE_{00} values, resulting in color changes, which are recognizable by naked eye. The CIE L*a*b* Color Studies revealed that the PDMS/GS/aero/N20 samples possess much better optical properties than those of the PDMS/ MMT/K/N20 samples.

3.1.2. Gloss values of the samples

Specular gloss is an important component of paper quality [40]. Gloss is frequently used to describe an object's surface's capacity to specularly reflect light. The term "delta gloss" describes the difference in gloss between the control and the coated samples. The delta gloss (Δ gloss) of the coated sample was calculated (Eq. 2) [20]. The Δ gloss of control and hybrid paper sheet samples is given in Table 4.

$$\Delta \text{ gloss } 75° = GC - GCP \quad (2)$$

where GC is the gloss of control paper and GCP is the gloss of coated paper. For delta gloss values at 75° among WFP/PDMSK/MMT/K/N20 samples, there is a trend towards increasing Δgloss values (= decreasing coated gloss) when the PDMS molecular weight in the coating is increased (except for WFP/PDMS-92K/ MMT/K/N20). The trend of decreasing coated closs values for the WFP/PDMS/GS/aero/N20 is not as pronounced as the trend among the WFP/PDMSK/ MMT/K/N20 samples.

Table 4: Optical properties of the coated samples.

Sample code	L*	a*	b*	ΔE00	Control gloss 75°	Coated gloss 75°	Delta gloss 75°
WFP/PDMS-6K (control)	95.0	0.2	2.8	-	16.65	16.25	0.40
WFP/PDMS-1.2K/GS/aero/N20	95.4	0.2	1.6	1.1	16.65	17.10	-0.45
WFP/PDMS-6K/GS/aero/N20	95.2	0.2	1.8	0.9	16.65	16.04	0.61
WFP/PDMS-9K/GS/aero/N20	95.4	0.2	2.1	0.7	16.65	15.46	1.19
WFP/PDMS-50K/GS/aero/N20	95.3	0.2	2.1	0.7	16.65	15.80	0.85
WFP/PDMS-92K/GS/aero/N20	95.0	0.2	3.0	0.2	16.65	15.38	1.27
WFP/PDMS-1.2K/MMT/K/N20	94.7	0.1	4.1	1.2	16.65	15.58	1.07
WFP/PDMS-6K/MMT/K/N20	94.2	0.2	5.1	2.0	16.65	15.58	1.07
WFP/PDMS-9K/MMT/K/N20	94.8	0.2	3.7	0.8	16.65	16.32	0.33
WFP/PDMS-50K/MMT/K/N20	94.3	0.7	-0.9	3.6	16.65	15.01	1.64
WFP/PDMS-92K/MMT/K/N20	94.4	0.6	-0.3	3.0	16.65	16.25	0.40

It was expected that rougher samples would have lower gloss values. When roughnesses of the sample (Tables 5 and 6) values were considered, it was noticed that this was not the trend in our samples [44-46]. When literature about the correlation between roughness and gloss values of the samples are considered, it is seen that such correlations are made for either inked/dyed or bare but homogenous surfaces. However, the sample surfaces in our study are heterogenous and composed of a mixture of polymeric and inorganic parts with a paper substrate underneath. Even the inorganic layer is composed of many different particles. So, it is not reasonable to expect an inverse relationship between the surface roughness and the gloss values.

3.2. Investigation of the physical properties

3.2.1. Bendtsen roughness values of the samples

An investigation of the paper roughness was performed using the Bendsten instrument. It is a pneumatic tool that gives an idea of the sample surface irregularity by detecting an air leak between a clamped paper substrate and the glass plate underneath. A rough surface results in a larger air leak and vice versa [47]. After conditioning the samples for 24 h at 23±2 °C and 50± 5 % relative humidity, the analyses were performed. At least five measurements were taken for each sample at room temperature.

Bendsten roughness values of the samples are listed in Table 5. WFP has the highest roughness value of 1212.7±23.4 mL/min, which did not change much upon PDMS coating. But hybrid paper sheets with filler particles in the coating formulation have significantly reduced Bendsten roughness. It is known that porous paper substrates have nano- to micron-sized voids. When only a PDMS coating was applied, the coating layer was not enough to fill the voids and reduce the roughness. In the presence of inorganic fillers, on the other hand, the coating layer partially fills the voids and reduces the roughness values.

3.2.2. Average roughness (Ra) determination

In this study, average roughness (Ra) values of the samples were determined by a confocal microscope for both correlation purposes of the measured data with the Bendsten roughness values and for a detailed investigation of the effect of the inorganic particles selected on the surface topography of the samples. For each sample, at least 10 250 × 250 μm^2 images were obtained using a Zeiss C Epiplan Apocromat 50×/0.95 DIC lens, and the Ra values calculated by the software were averaged. A list of the data and the corresponding % frequency values are given in Table 6.

Table 5: Air permeance and Bendsten roughness values of the samples.

Sample code	Air permeance (mL/min)	Bendsten surface roughness (mL/min)
WFP/PDMS-6K (control)	3675.0±49.5	1277.0±19.8
WFP/PDMS-1.2K/GS/aero/N20	1857.0±19.8	877.0±38.2
WFP/PDMS-6K/GS/aero/N20	2885.0±17.1	726.5±53.0
WFP/PDMS-9K/GS/aero/N20	1705.0±48.5	685.0±71.9
WFP/PDMS-50K/GS/aero/N20	2015.0±49.5	646.5±36.1
WFP/PDMS-92K/GS/aero/N20	1939.1±73.5	904.5±67.5
WFP/PDMS-1.2K/MMT/K/N20	1455.0±21.2	816.0±81.5
WFP/PDMS-6K/MMT/K/N20	529.5±34.6	837.0±18.4
WFP/PDMS-9K/MMT/K/N20	563.5±12.0	801.8±92.4
WFP/PDMS-50K/MMT/K/N20	637.5±21.9	827.2±87.4
WFP/PDMS-92K/MMT/K/N20	597.5±65.8	1078.5±47.8

Table 6: Average Ra values and the corresponding % frequencies of the samples.

Code	ave. Ra (µm)	std. dev. (µm)	Value range (µm)	no. of meas.	% frequency	Code	ave. Ra (µm)	std. dev. (µm)	Value range (µm)	no. of meas.	Frequency %
WFP	4.37	1.67	0.00-1.00	0	0	WFP/PDMS-6K	2.90	1.02	0.00-1.00	0	0
			1.00-2.00	1	10				1.00-2.00	0	0
			2.00-3.00	1	10				2.00-3.00	4	40
			3.00-4.00	3	30				3.00-4.00	4	40
			4.00-5.00	2	20				4.00-5.00	1	10
			5.00-6.00	0	0				5.00-6.00	1	10
			6.00-7.00	1	10				6.00-7.00	0	0
			7.00-8.00	1	10				7.00-8.00	0	0
			8.00-9.00	0	0				8.00-9.00	0	0
			9.00-10.00	1	10				9.00-10.00	0	0
WFP/PDMS-1.2K/GS/aero/N20	3.37	1.44	0.00-1.00	0	0	WFP/PDMS-1.2K/MMT/K/N20	2.98	1.11	0.00-1.00	0	0
			1.00-2.00	1	10				1.00-2.00	1	10
			2.00-3.00	4	40				2.00-3.00	4	40
			3.00-4.00	3	30				3.00-4.00	3	30
			4.00-5.00	1	10				4.00-5.00	1	10
			5.00-6.00	0	0				5.00-6.00	1	10
			6.00-7.00	1	10				6.00-7.00	0	0
			7.00-8.00	0	0				7.00-8.00	0	0
			8.00-9.00	0	0				8.00-9.00	0	0
			9.00-10.00	0	0				9.00-10.00	0	0
WFP/PDMS-6K/GS/aero/N20	3.98	0.98	0.00-1.00	0	0	WFP/PDMS-6K/MMT/K/N20	2.19	0.49	0.00-1.00	0	0
			1.00-2.00	0	0				1.00-2.00	3	30
			2.00-3.00	1	10				2.00-3.00	7	70
			3.00-4.00	4	40				3.00-4.00	0	0
			4.00-5.00	4	40				4.00-5.00	0	0
			5.00-6.00	0	0				5.00-6.00	0	0
			6.00-7.00	1	10				6.00-7.00	0	0
			7.00-8.00	0	0				7.00-8.00	0	0
			8.00-9.00	0	0				8.00-9.00	0	0
			9.00-10.00	0	0				9.00-10.00	0	0
WFP/PDMS-9K/GS/aero/N20	2.58	0.54	0.00-1.00	0	0	WFP/PDMS-9K/MMT/K/N20	3.33	1.15	0.00-1.00	0	0
			1.00-2.00	2	20				1.00-2.00	1	10
			2.00-3.00	5	50				2.00-3.00	2	20
			3.00-4.00	3	30				3.00-4.00	4	40
			4.00-5.00	0	0				4.00-5.00	2	20
			5.00-6.00	0	0				5.00-6.00	1	10
			6.00-7.00	0	0				6.00-7.00	0	0
			7.00-8.00	0	0				7.00-8.00	0	0
			8.00-9.00	0	0				8.00-9.00	0	0
			9.00-10.00	0	0				9.00-10.00	0	0

Table 6: Continue.

Code	ave. Ra (µm)	std. dev. (µm)	Value range (µm)	no. of meas.	% frequency	Code	ave. Ra (µm)	std. dev. (µm)	Value range (µm)	no. of meas.	Frequency %
WFP/PDMS-50K/GS/aero/N20	2.44	0.60	0.00-1.00	0	0	WFP/PDMS-50K/MMT/K/N20	2.04	0.82	0.00-1.00	0	0
			1.00-2.00	2	20				1.00-2.00	4	40
			2.00-3.00	6	60				2.00-3.00	4	40
			3.00-4.00	2	20				3.00-4.00	2	20
			4.00-5.00	0	0				4.00-5.00	0	0
			5.00-6.00	0	0				5.00-6.00	0	0
			6.00-7.00	0	0				6.00-7.00	0	0
			7.00-8.00	0	0				7.00-8.00	0	0
			8.00-9.00	0	0				8.00-9.00	0	0
			9.00-10.00	0	0				9.00-10.00	0	0
WFP/PDMS-92K/GS/aero/N20	2.88	0.68	0.00-1.00	0	0	WFP/PDMS-92K/MMT/K/N20	2.60	1.15	0.00-1.00	0	0
			1.00-2.00	0	0				1.00-2.00	3	30
			2.00-3.00	6	60				2.00-3.00	2	20
			3.00-4.00	3	30				3.00-4.00	4	40
			4.00-5.00	1	10				4.00-5.00	1	10
			5.00-6.00	0	0				5.00-6.00	0	0
			6.00-7.00	0	0				6.00-7.00	0	0
			7.00-8.00	0	0				7.00-8.00	0	0
			8.00-9.00	0	0				8.00-9.00	0	0
			9.00-10.00	0	0				9.00-10.00	0	0

When Table 6 and Figure 1 are studied, it can be concluded that the Ra values of the WFP/PDMS/GS/aero/N20 samples decrease as the molecular weight of PDMS in the coating formulation increases. Moreover, the Ra frequency value distributions and, thus, the histogram graph distributions of the samples narrow down. It can be said that increasing PDMS molecular weight results in relatively homogenous surface roughness values on sample surfaces, which contain only spherical inorganic particles in the coating formulation.

Table 6 and Figure 2 reveal that the effect of the increase in the molecular weight of PDMS in the coating formulation of the WFP/PDMS/MMT/K/N20 on Ra values, Ra frequency value distributions and the corresponding histogram graph distributions, is not as significant as in the WFP/PDMS/GS/aero/N20 samples. It can be said that the PDMS molecular weight has no extra effect on the surface roughness, which is already found to be relatively homogeneous with respect to the WFP/PDMS/GS/aero/N20 samples.

Moreover, it is important to report that the trend between PDMS molecular weight and roughness values detected both with the Bendsten instruments and a confocal microscope is similar: As the molecular weight of PDMS in the coating formulation of the WFP/PDMS/GS/aero/N20 samples increases, the roughness values of the samples decrease. However, the effect of the increase in the molecular weight of PDMS in the coating formulation of the WFP/PDMS/MMT/K/N20 on Ra values is not as significant as in the WFP/PDMS/GS/aero/N20 samples.

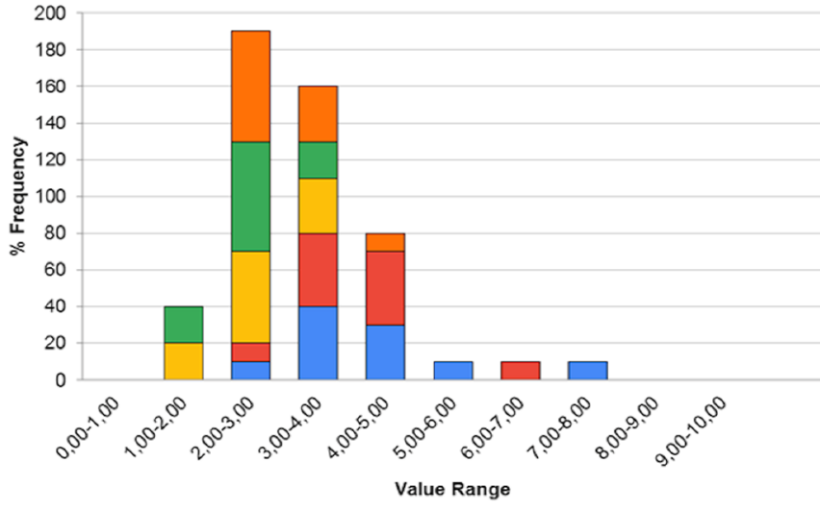

Figure 1: Histogram graphs of Ra frequency (%) values for WFP/PDMS-1.2K/GS/aero/N20, WFP/PDMS-6K/GS/aero/N20, WFP/PDMS-9K/GS/aero/N20, WFP/PDMS50K/GS/aero/N20, and WFP/PDMS-92K/GS/aero/N20.

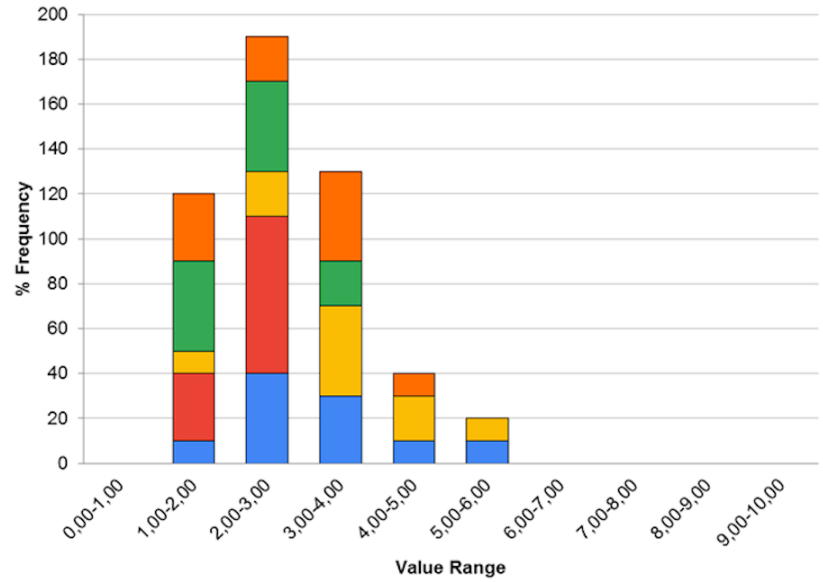

Figure 2: Histogram graphs of Ra frequency (%) values for WFP/PDMS-1.2K/MMT/K/N20, WFP/PDMS-6K/MMT/K/N20, WFP/PDMS-9K/MMT/K/N20, WFP/PDMS50K/MMT/K/N20, and WFP/PDMS-92K/MMT/K/N20.

3.3. Investigation of the barrier properties

3.3.1. Air permeance values of the samples

Barrier performances of the hybrid paper sheets against air were performed by using a L&W Air Permeance Tester according to the Gurley method, which basically determines the air resistance of paper and/or paper-based material in the presence of a pressure differential between two sides of it. After conditioning the samples for 24 h at 23 ±2 °C and 50 ± 5 % relative humidity, at least 5 measurements were taken for each sample at room temperature [48]. The values are listed in Table 5. WFP has the highest air permeance with 3550.0 ± 127.3 mL/min, which is expected. WFP/PDMS-6K has a highly similar air permeance value to that of WFP. However, all the hybrid paper sheets have lower air permeances than those of the WFP or WFP/PDMS-6K. Here, it is important to note that the platelet-shaped filler particles are much more efficacious in enhancing the air barrier properties of the samples, which was also reported in our previous work [15]. The effect of PDMS molecular weight used in the coating formulation does not have a significant effect on the air permeance values of the hybrid paper sheets when only spherical (colloidal and fumed) inorganic particles are present in the coating. In the case of hybrid paper

sheets with platelet-shaped particles, on the other hand, WFP/PDMS-1.2K/MMT/K/N20 has a significantly higher air permeance than that of the others. It is quite possible that shorter PDMS chains are not enough to fill the voids between platelet-shaped inorganics. Although there is a decrease in air permeance with the coating application for the superhydrophobic paper sheets, it can be concluded that the coating layers do not behave as an air barrier and still enable breathing of the filter paper underneath.

3.3.2. Water barrier properties of the samples

Cobb tests, known as a measure for water absorprtiveness of paper and paper-based materials, are often used to calculate the mass of water absorbed by one square meter of sample at a given time [49-51]. Cobb values of the sample were calculated (Eq. 3), in which the sample area is fixed at 0.01 m^2. At least 5 measurements were taken for each sample at room temperature.

Cobb value (g/m^2) = (weight of the wet sample - weight of the dry sample)/sample area (3)

Additionally, the test was carried out by using 100 mL of distilled water at 90 °C in order to investigate the water absorptiveness of samples at elevated temperatures of water. The Cobb test results (g/m^2) of the samples are given in Table 7. Additionally, the percent decrease in Cobb values is calculated.

The PDMS layer on the control sample is not very effective in decreasing the Cobb value of WFP. However, when tests are examined at 23 ± 2 °C, there is a significant decrease above 90 % in the Cobb values of the hybrid paper sheets, irrespective of the PDMS molecular weight in the coating formulation, both for the WFP/PDMS/GS/aero/N20 and WFP/MMT/K/N20 samples.

When distilled water at 90 ± 2 °C is used to test the water absorptiveness of the samples, the trend changes: The Cobb values of the WFP/PDMS/GS/aero/N20 samples decrease with increasing PDMS molecular weight in the coating formulation. And increased water temperature increases the Cobb values of hybrid paper sheets calculated at 90 °C. At this stage, it is important to observe the effect of PDMS molecular weight on the final properties at elevated water temperatures.

Table 7: Cobb values of the samples with the calculated % decrease in Cobb Values.

Sample Code	water at 23 ± 2 °C (RT)		water at 90 ± 2 °C	
	ave. Cobb Value (g/m^2)	% decrease in Cobb value	ave. Cobb Value (g/m^2)	% decrease in Cobb value
WFP	249.0 ± 11.8	-	255.8 ± 8.2	-
WFP/PDMS-6K	223.5 ± 5.5	-10.3	226.0 ± 13.2	-11.6
WFP/PDMS-1.2K/GS/aero/N20	12.4 ± 2.2	-95.0	185.2 ± 45.2	-27.6
WFP/PDMS-6K/GS/aero/N20	11.3 ± 2.8	-95.5	111.4 ± 18.7	-56.5
WFP/PDMS-9K/GS/aero/N20	9.1 ± 1.0	-96.4	133.3 ± 74.7	-47.9
WFP/PDMS-50K/GS/aero/N20	8.4 ± 1.9	-96.6	86.1 ± 24.2	-66.4
WFP/PDMS-92K/GS/aero/N20	10.0 ± 3.5	-96.0	61.8 ± 10.7	-77.0
WFP/PDMS-1.2K/MMT/K/N20	9.9 ± 0.6	-96.0	50.3 ± 10.4	-80.3
WFP/PDMS-6K/MMT/K/N20	10.7 ± 2.0	-95.7	120.2 ± 66.3	-53.0
WFP/PDMS-9K/MMT/K/N20	5.6 ± 0.6	-97.8	100.8 ± 41.3	-60.6
WFP/PDMS-50K/MMT/K/N20	6.4 ± 1.2	-97.4	72.2 ± 7.4	-71.8
WFP/PDMS-92K/MMT/K/N20	9.0 ± 3.6	-96.4	59.3 ± 7.2	-76.8

The Si-O and Si-C bonds in PDMS are significantly longer than the C-C bonds that make up most polymers. Besides, because of the ~51 % ionic character of the Si-O bonds, PDMS chains have high flexibility and mobility, which are not seen in most polymer chains [1]. The increase in temperature seems to influence the mobility and swelling ability of the PDMS chains, although the solubility of water in PDMS is very low, less than 1 ppm [1, 52]. It is possible that the presence of inorganic particles endows PDMS swelling ability in water [53]. So, water can penetrate through the thin superhydrophobic coating with increasing temperature, which then also results in swelling and more water uptake of the cellulose domains making up the WFP substrate umderneath. For WFP/MMT/K/N20 samples, on the other hand, no relation between Cobb values and the PDMS molecular weight could be found, in accordance with the previous findings. But increased water temperature also increases the Cobb values of WFP/MMT/K/N20 samples, as expected.

The durability of the hybrid sheets against water both at RT and at high temperatures (when compared to that of the WFP), combined with our previous studies revealing the durability of these samples at elevated temperatures up to 200 °C for 3 hours, is a very promising outcome since the hybrid paper sheets are thought of as promising alternatives to packaging materials [16].

3.4. ATR-IR studies

The determination and interpretation of the bonds between the paper and the coating mixture are important to understand the chemical properties of the materials prepared in this study. Since the interaction between the coating layer and the paper substrate takes place in a solvent-free environment, there is no need to talk about double-layer forces during sample preparation. PDMS in the coating mixture contains Si-O-Si and Si-C bonds, which are known to be longer than the C-C bonds found in most polymers. Moreover, Si-O bonds have a 51 % ionic character. Due to these properties of the bonds, PDMS chains have very high mobility. Therefore, it is thought that there is no steric hindrance that would affect the covalent bonds that may form between -O- or -OH groups and -Si- on the paper surface [1]. Possible covalent bonding mechanisms are (i) water-assisted hydrolysis of PDMS followed by condensation with hydroxyl groups on the substrate surface (right) and (ii) direct or acid-catalyzed silanolysis of PDMS by hydroxyl groups on the substrate surface, as described in previous publications and summarized in Figure 3 [12]. The figure adapted from the work of Krumpfer and McCarthy is also suitable for the possible mechanisms between the hydrophilic and slightly acidic paper substrate and the PDMS chains: Hydroxyl groups and siloxane units on the surface of the paper substrate have the tendency to react, leading to the formation of Si-O-C bonds. Since Si (and C in the methyl groups) on PDMS chains have a partial positive charge (δ^+), they are also likely to undergo dipole-dipole interactions with the partially negative charge (δ^-) of -OH groups on paper and inorganic particles. Furthermore, H-bonds are expected to form between the -O- on the PDMS chain and the -OH groups on the paper and inorganic particles. The surface of the inorganic particles used is also known to exhibit acidic properties. It is also possible that the negative surface charges of both paper and inorganic particles are partially attached to positively charged Si or -CH_3 groups by steric effects.

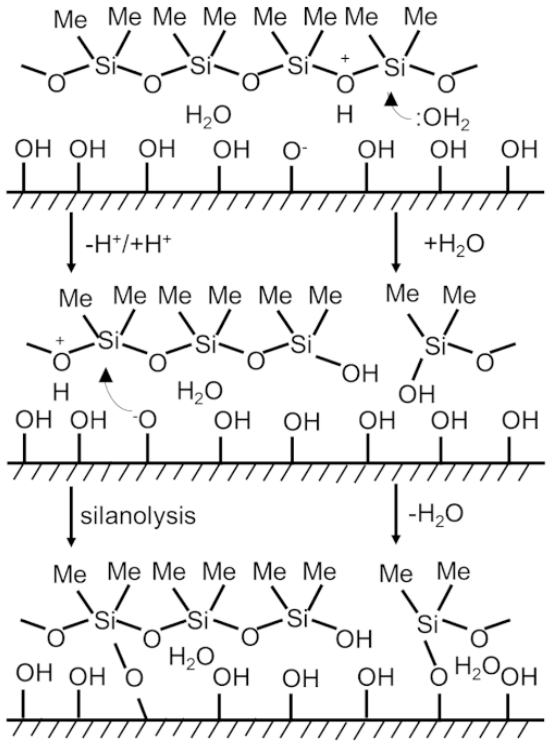

Figure 3: Possible covalent bonds between PDMS chains and paper surface.

In this study, the chemistry of WFP and hybrid paper sheet surfaces was also examined by FT-IR measurements. The spectra of the samples are given in Figures 4, 5, and 6. First, the spectra of WFP, WFP/PDMS-6K/GS/aero/N20, and WFP/PDMS-6K/ MMT/K/N20 were compared. Then, the spectra of the samples with varying PDMS molecular weights in the coating formulation were analyzed.

As revealed in Figure 4 A and B, WFP has peaks at 3332 and 3273 cm^{-1} due to the presence of -OH groups on its surface. Moreover, the peaks at 1054 and 1031 cm^{-1} correspond to the C-OH stretches of the secondary alcohol and primary alcohol groups of the cellulose backbone, respectively [54, 55]. The peak at 1111 cm^{-1} corresponds to the C-O-C stretch. In the spectra of WFP/PDMS-6K/GS/aero/N20 and WFP/ PDMS-6K/ MMT/K/N20, the intensity of the peaks at 3332, 3273, 1054, and 1031 cm^{-1} decreases significantly, which is an indication of a reaction between the hydroxyl groups on the paper substrate surface and the coating on top.

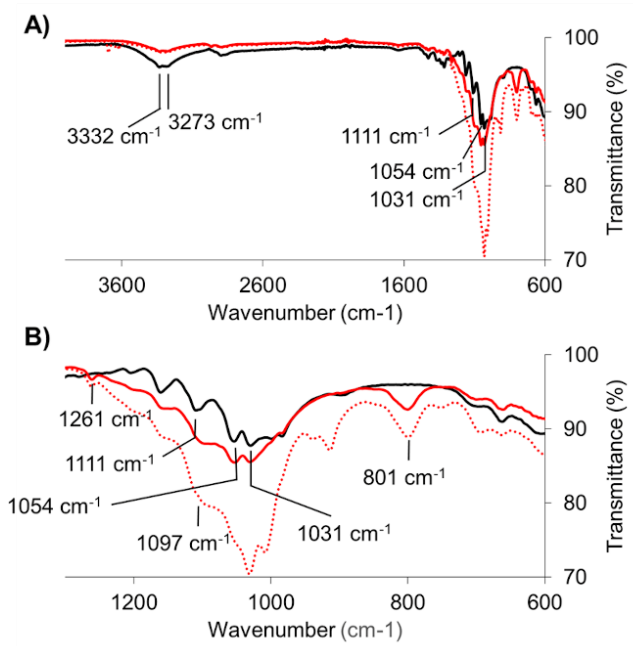

Figure 4: FT-IR spectra of WFP (___), WFP/PDMS-6K/GS/aero/N20 (___), and WFP/PDMS-6K/MMT/K/N20 (…..) in A) 4000-600 and B) 1300-600 cm^{-1} range.

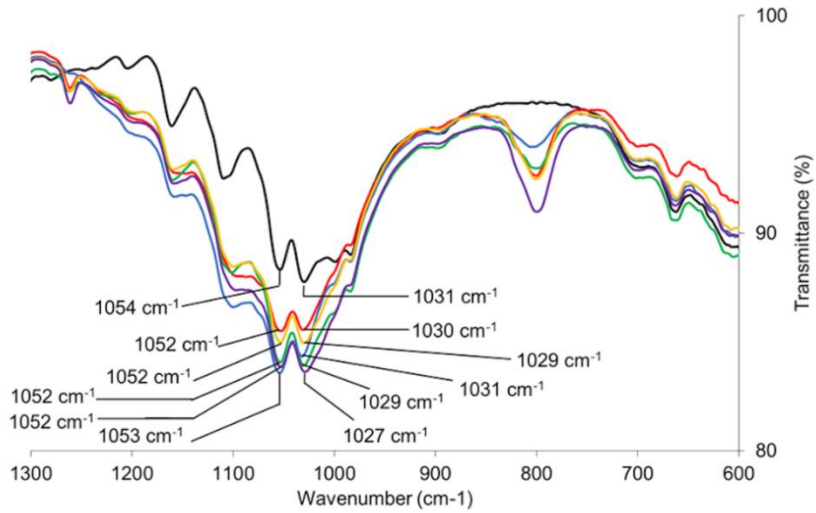

Figure 5: FT-IR spectra of WFP (___), WFP/PDMS-1.2K/GS/aero/N20 (___), WFP/PDMS-6K/GS/aero/N20 (___), WFP/PDMS-9K/GS/aero/N20 (___), WFP/PDMS-50K/GS/aero/N20 (___), WFP/PDMS-92K/GS/aero/N20 (___) in 1300-600 cm^{-1} range.

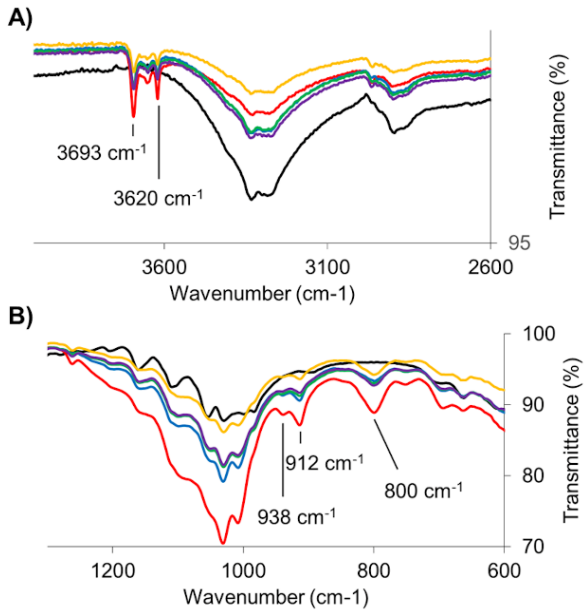

Figure 6: FT-IR spectra of WFP (___), WFP/PDMS-1.2K/MMT/K/N20 (___), WFP/PDMS-6K/MMT/K/N20 (___), WFP/PDMS-9K/MMT/K/N20 (___), WFP/PDMS-50K/MMT/K/N20 (___), WFP/PDMS-92K/MMT/K/N20 (___) in A) 4000-2600 and B) 1300-600 cm^{-1} range.

The peak for the C-OH stretches of secondary alcohol groups on WFP has the highest intensity, with 88.3 % transmittance and 90.5 % relative intensity with respect to the peak at 2896 cm^{-1} assigned to the asymmetric $-CH_2$ stretch. The same peak on the secondary alcohol present in the WFP/PDMS-6K/GS/aero/N20 spectrum is less intense, with a % transmittance value of 85.5 and a relative intensity of 86.6. The C-OH stretch of secondary alcohol groups on WFP/PDMS-6K/MMT/ K/N20 has the lowest intensity, with 75.0 % transmittance and 76.0 % relative intensity. The peak for the C-OH stretches of primary alcohol groups at 1031 cm^{-1} has the highest intensity with 87.8 % transmittance and 89.9 % relative intensity, which diminishes to 85.6 % transmittance (86.7 % relative intensity) for WFP/PDMS-6K/GS/ aero/ N20 and 70.5 % transmittance (71.4 % relative intensity) for WFP/ PDMS-6K/MMT/K/N20.

In the spectra of both hybrid paper sheets, fresh peaks at 1261, 1097, and 801 cm^{-1} emerge. The peak at 1261 cm^{-1} is known as the symmetric $-CH_3$ deformation of the PDMS backbone [56]. The broad peak at 1097 cm^{-1} is thought to be a combination of the C-O-C stretch of cellulose, the Si-O-Si stretch of PDMS units, the Si-O-Si stretch of inorganic particles, and the freshly formed Si-O-C bonds [57-59]. Moreover, the shift of the C-O-C peak to lower wavenumbers might also be an indication of H-bonding between the ether oxygen in the cellulose backbone and -OH groups of the inorganics present in the coating formulation. And the peak at 801 cm^{-1} corresponds to the Si-O stretching and reveals the presence of inorganics in the coating formulation [60].

At this stage, it is important to point out that the bonding character between PDMS and cellulose chains was further investigated by Raman studies previously [29]. Briefly, model compounds of microcrystalline cellulose (MCC) and PDMS were prepared by mixing and subsequent heat treatment at 120 °C. Raman spectra of PDMS, MCC, and the model compound of MCC/PDMS revealed that there are additional peaks at 1161 and 806 cm^{-1} in the spectrum of MCC/PDMS, which correspond to the freshly formed Si-O-C asymmetric and asymmetric stretching peaks, respectively [61].

When the spectra of the WFP/PDMS/GS/aero/N20 samples with different PDMS molecular weights (sample #s 2 to 6 in Table 3) are compared, a slight shift in the peak positions of 1054 and 1031 cm^{-1} is seen besides the decrease in intensities of those. This shift is an indication of H-bonding between the Si-O-Si gropus of the PDMS backbone or Si-O-Si groups of the inorganics found in the coating and the free OH groups of the WFP, which is more pronounced with increasing PDMS molecular weight. The secondary -OH peak of WFP positioned at 1054 cm^{-1} is shifted to 1053 cm^{-1} for WFP/PDMS-1.2K/GS/aero/N20 and to 1052 cm^{-1} for

the other WFP/PDMS/GS/aero/N20 samples. The primary OH peak positioned at 1031 cm^{-1} is shifted to 1030 cm^{-1} for WFP/PDMS-6K/GS/aero/N20, to 1029 cm^{-1} for WFP/PDMS-9K/GS/aero/N20 and WFP/PDMS-50K/GS/aero/N20, and to 1027 cm^{-1} for WFP/PDMS-92K/GS/aero/N20. It is quite possible that the increased chain length linking the inorganic filler particles to each other and to the WFP substrate surface enables an increase in H-bonds.

When the spectra of the WFP/PDMS/MMT/K/N20 samples (sample #s 7 to 11 in Table 3) are investigated, it is seen that the secondary -OH peak intensity diminishes significantly in the spectra, which looks more like a shoulder than a peak. Also, a slight shift to lower wavenumbers is observed, the effect of PDMS molecular weight on which is not as clear as that of the WFP/PDMS/GS/aero/N20 samples. It is also important to point out that there is a change in the characteristic -OH stretching vibrations of kaolin, revealing its triclinic layer structure: Pure kaolin possess -OH stretching peaks at 3652, 3671, and 3694 cm^{-1} because of the presence of its outer -OH groups, and a peak at 3620 cm^{-1} corresponds to its inner -OH groups. The presence of these peaks corresponds to its crystalline structure. The spectra of hybrid paper sheets, on the other hand, have just a slight peak at 3693 cm^{-1} and a peak at 3620 cm^{-1}. The disappearance of the other -OH stretching vibrations can be an indication of a slight change in kaolin structure in hybrid samples [62-64]. The peak at 912 cm^{-1} is a combination of stretches and bends belonging to MMT and kaolin, respectively. Moreover, the peak at 938 cm^{-1} corresponds to the inner -OH groups of kaolin. And the distinct peak at around 800 cm^{-1} is an indication of the presence of N20 and MMT in the coating formulation [60, 65].

3.5. SEM Studies

3.5.1. SEM studies of model compounds

In this study, model samples of platelet-shaped filler particles dispersed in THF were also prepared in order to observe the distribution of these inorganic particles on the surfaces after the spray-coating procedure. It was investigated whether the particles are homogenously dispersed on the surface and/or present in an agglomerated state. The platelet-shaped filler particle dispersions were spray-coated on 2×2 cm^2 glass slide surfaces in order to eliminate the surface structures of fibrous and thus rough paper substrates. Briefly, the dispersions were transferred to the tank of the spray gun, and the glass slide substrates were spray-coated at a tank pressure of around 2 bars. The distance between the nozzle and the glass slide was fixed at 20 cm. The wt. % inorganic particle ratio of the model sample mixtures was kept the same as the wt. % inorganic particle ratio of the PDMS-containing coating sample mixtures (Table 1). For ease of comparison of the particle behavior on the surfaces of the model samples with those on the surfaces of the hybrid paper sheets, KN5 is also prepared, which contains fumed silica (N20) besides the mixture of MMT and K.

SEM images of M-SEM-MMT are given in Figure 7 A and B, which reveal that particles are homogeneously distributed on the surface. However, the sizes of the particles range from a few hundred nanometers to 30 micrometers. It is already known in the literature that each MMT platelet is composed of many MMT sheets [66-68]. Thus, it can be concluded that the MMT particles are found mostly in agglomerated form, and the method used is not sufficient to exfoliate MMT platelets and/or sheets. However, it is thought that these agglomerated MMT particles result in the high barrier and low wetting properties observed in previous studies by helping to close the pores on the paper surface with diameters ranging from 20 to 100 μm.

Figure 7 C and D reveal the SEM images of M-SEM-K. K particles of sizes ranging from approximately 700 nm to 5 μm appear to be homogeneously distributed on the surface. Therefore, it was determined that the mixture preparation and subsequent spraying method applied allowed the particles to be homogeneously distributed on the surface. The plate appearance and size of kaolin particles coincide with the information reported in the literature [69, 70]. It is reported in the relevant literature that each plate consists of approximately 10-50 fine plate grains overlapping, and WAXD studies of these aggregate structures within the scope of our study are described in the following paragraphs.

SEM images of M-SEM-MMT/K/N20 are given in Figure 7 E and F. It can be seen that the mixture of MMT, K, and N20 particles homogeneously covers the glass slide, and aggregated particles are dispersed on the surface. These particles range in size from a few hundred nanometers to about 40 micrometers, and characteristic plate images can still be distinguished for some particles, although the whole surface is covered with N20 particles (Figure 7 F).

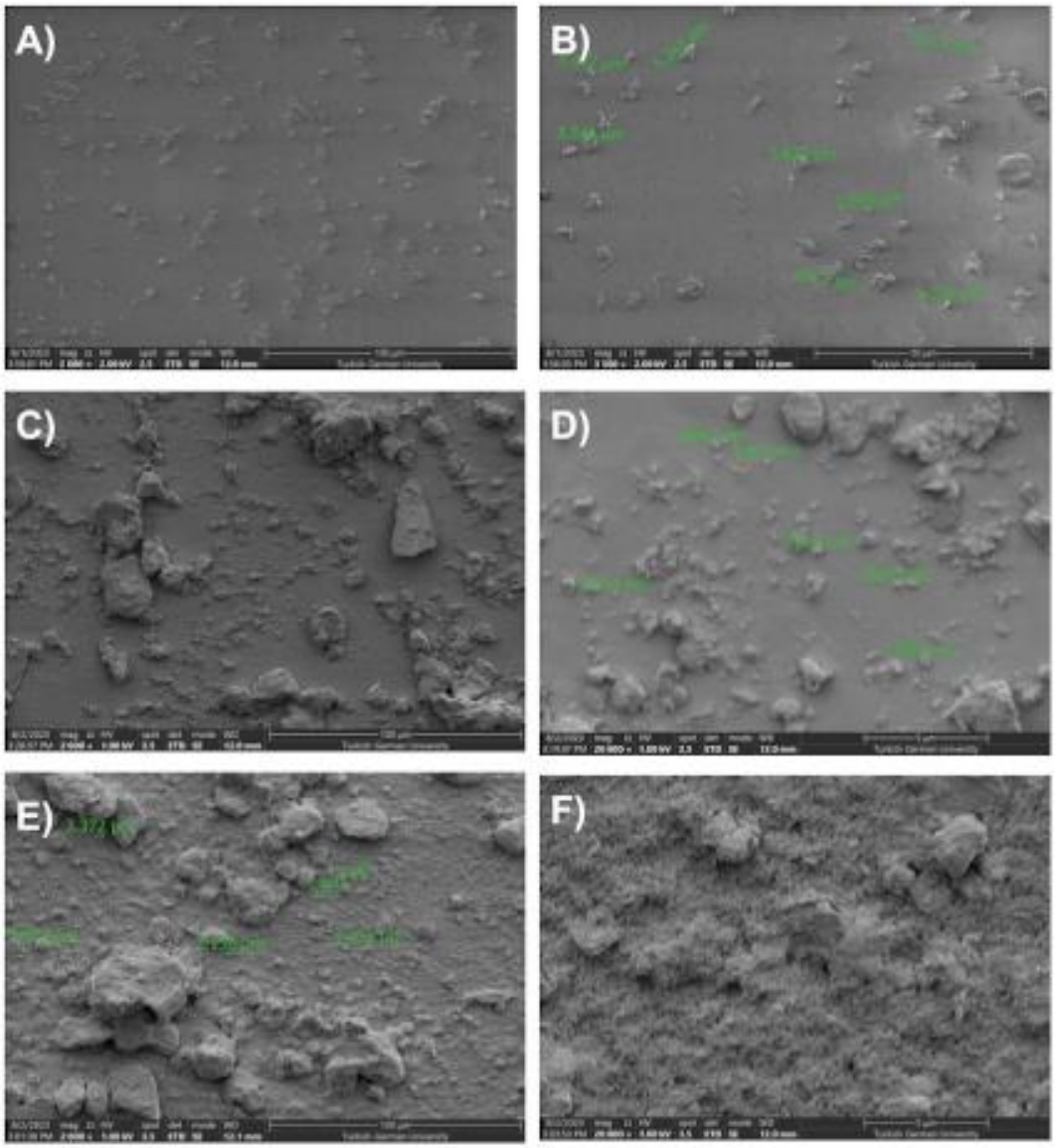

Figure 7: SEM images of M-SEM-MMT showing the distribution and size of MMT particles at A) 2000X and B) 20000X magnification levels. SEM images of M-SEM-K showing C) distribution and D) size of kaolin particles. SEM images of M-SEM-MMT/K/N20 at A) 2000X ve B) 20000X magnification levels.

3.5.2. SEM studies of hybrid paper sheets

In order to reveal the significant differences in the surface topography of the control sample and the different hybrid paper sheets, SEM examinations were performed. Images were taken at an accelerating voltage of 2 kV and in secondary electron (SE) mode. The morphologies of the surfaces were examined using a magnification range of 2000 to 40000 ×. SEM images of the samples are shown in Figure 8.

SEM images revealed that the specific fibrillar structure of the filter paper can still be detected on the surface of the control sample. On the other hand, in hybrid paper sheets, the paper substrate surface is covered by the coating layer, and the cellulose fibers are barely visible under the coating. The dense distribution of filler particles of different sizes is also clearly visible on the hybrid paper sheet surfaces. This distribution of micro- and nano-sized surface structures is very similar to that on the surface of the Lotus plat leaves, resulting in a superhydrophobic behavior of the sample surface [71]. The surface of the filter paper selected for this study was also examined in previous studies, and it was observed that pore diameters can vary between 20 and 100 micrometers [15]. The pores on the control sample surface were also in this size range. On hybrid paper sheet surfaces, on the other hand, the size of these pores

was up to 20 micrometers and tended to decrease with increasing PDMS molecular weight in the coating formulation. The samples having PDMS with a molecular weight of 91700 g/mol in the coating, for example, have almost no pores, irrespective of the type of filler particles.

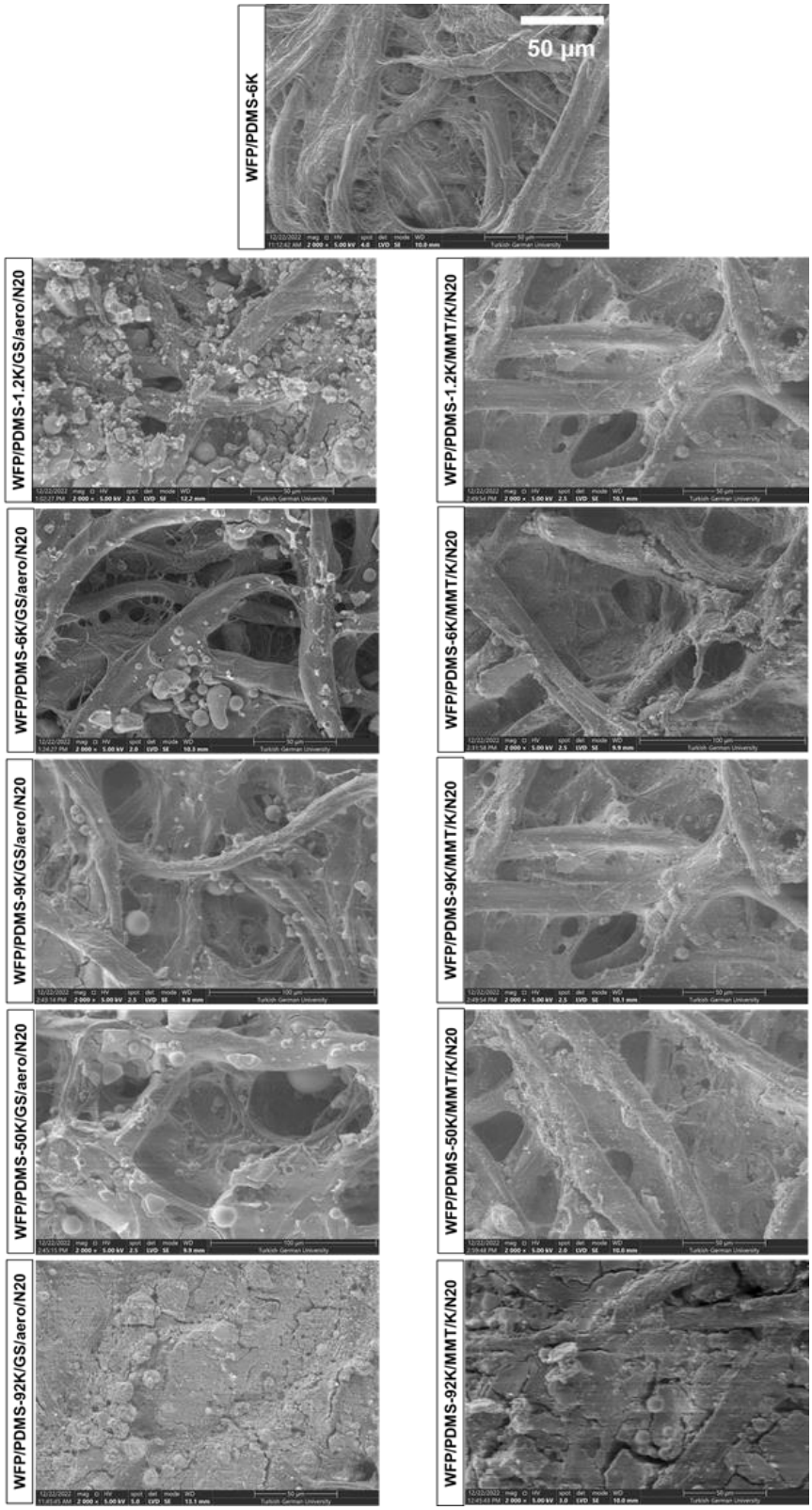

Figure 8: SEM images of the control sample and hybrid paper sheets at 2000 × magnification level.

In surface SEM-EDS analyses of the samples, the presence of Si atoms in the PDMS-based coating was examined both by elemental mapping and EDS spectra, as shown in Figure 9. The analysis of the control samples shows that there are Si elements of PDMS on the fibers and also in the holes of the membraneous paper surface, revealing that the sample is coated with a polymeric layer. Furthermore, the surfaces of all hybrid paper sheets were homogeneously coated with PDMS-based coatings, regardless of the coating formulation. The presence of Si atoms in the pores was also demonstrated by the EDS maps. The EDS spectra of the samples revealed the peaks of C, O, and Si. C and O are present in the cellulose backbone of the paper substrate. Si peaks, on the other hand, come from the coating possessing both the PDMS and Si-containing inorganic particles. Peaks of Na or Al present on the spectra belong to the impurities.

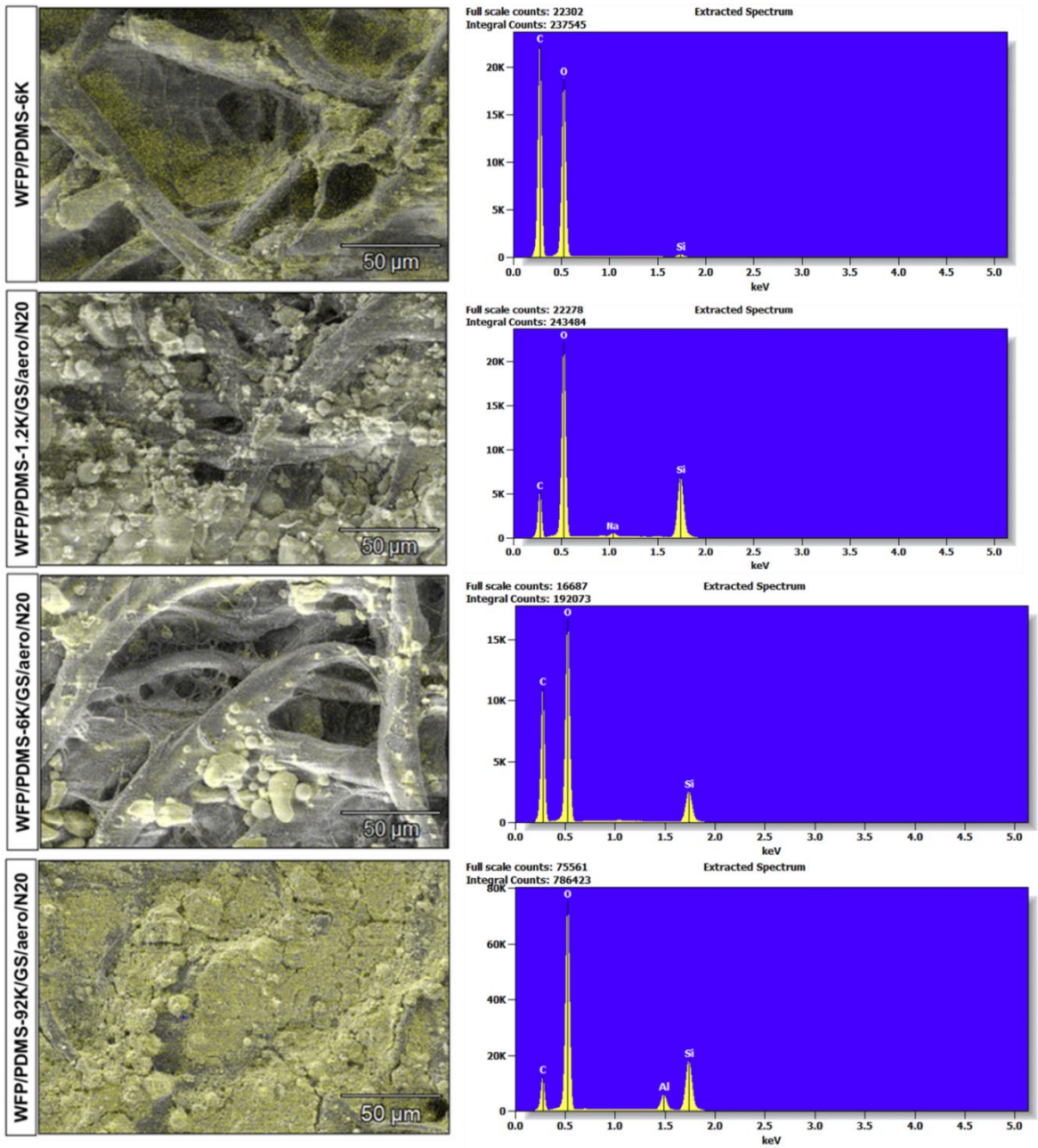

Figure 9: EDS analyses revealing Si mapping and EDS Spectra of WFP/PDMS-6K (control), WFP/PDMS-1.2K/GS/aero/N20, WFP/PDMS-6K/GS/aero/N20, and WFP/PDMS-92K/GS/aero/N20. The presense of Si elements is shown with yellow dots.

The SEM images of the samples containing only spherical particles in the coating layer and of those containing both spherical and platelet-shaped particles in the coating layer are also investigated at high magnification levels (20000 to 40000×) in order to see the effect of filler type in the coating formulation on the surface topographies of the samples (Figure 10). The platelet-shaped filler particles embedded into the fumed silica layer on the WFP/PDMS-92K/MMT/K/N20 surface, for example, have sizes ranging from several hundred nanometers up to 2 μm. The surfaces of the WFP/PDMS/GS/aero/N20 samples, on the other hand, only contain spherical particles.

3.6. Studies on the structural changes in model compounds via WAXD analyses

For the WAXD analyses, 0.1542 nm Cu-Kα radiation was used as the X-ray beam, and the divergence slit was fixed at 0.5 °. The scans were performed from 2θ= 2° up to 90° for MMT-containing samples and from 2θ=5 ° up to 90 ° for K-containing samples. The XRD intensities obtained were plotted against the scattering angle 2θ. The WAXD spectra of commercial kaolin (M-WAXD-K-no treatment), kaolin dispersed in THF (M-WAXD-K), and the kaolin/PDMS model compound (M-WAXD-PDMS-6K/K) are given in Figure 11 A. There is almost no change in the position of the peak detected at 2θ = 12.33° for M-WAXD-K-no treatment, which is assigned to the d(001) spacing of kaolin [65]. Moreover, a significant change could not be detected in the 2θ = 20–30 ° region, which is reported to give information about structural changes in kaolin. The crystallinity of kaolin can be evaluated on the basis of changes in peak positions in that region [72-74]. However, we also prepared model samples with varying PDMS molecular weights, as shown in Table 8. The 2θ peaks at around 12 and 20° reveal a shift toward lower numbers, revealing a slight change in the kaolin structure present in the model compound. Together with the ATR-IR results, it can be concluded that the method proposed for the sample and model compound preparation might result in a slight change in the kaolin structure. It is important to point out that the platelet-shaped particles remain unexfoliated or intercalated on the sample surfaces. Still, we could manage to get the nonwettable hybrid sheets with highly promising water barrier properties.

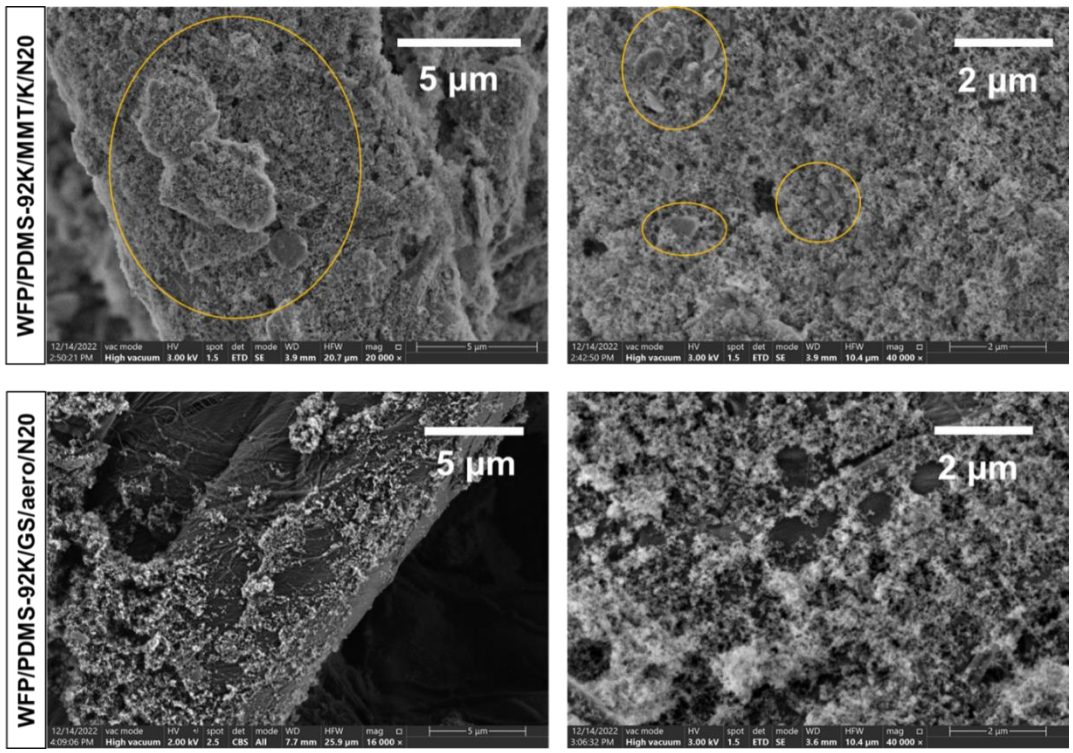

Figure 10: SEM images of WFP/PDMS-92K/MMT/K/N20 (some of the platelet shaped particles were shown in yellow circles) and WFP/PDMS-92K/GS/aero/N20 at different magnification levels.

Table 8: Peak positions on the XRD Spectra of model compounds.

Code	M-WAXD-PDMS-1.2 K/K	M-WAXD-PDMS-6 K/K	M-WAXD-PDMS-9 K/K	M-WAXD-PDMS-50 K/K	M-WAXD-PDMS-92 K/K
2θ peak position (°)	12.60	12.45	12.43	12.35	12.35
	20.15	20.03	19.95	19.85	19.91
	24.94	24.94	24.95	24.84	24.84

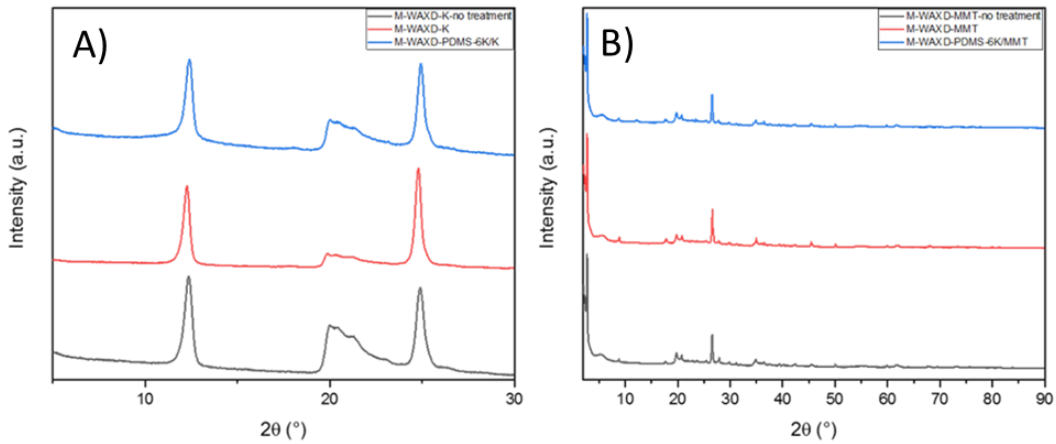

Figure 11: XRD patterns of A) M-WAXD-K-no treatment, M-WAXD-K, and M-WAXD-PDMS-6K/K and B) M-WAXD-MMT-no treatment, M-WAXD-MMT, and M-WAXD-PDMS-6K/MMT.

The WAXD spectra of commercial montmorillonite (M-WAXD-MMT-no treatment), montmorillonite dispersed in THF (M-WAXD-MMT), and the MMT/PDMS model compound (M-WAXD-PDMS-6K/MMT) are given in Figure 11 B. Montmorillonite peaks correlate well with the ones reported in the literature, including 2θ=12.5° for (001), 2θ = 20.6° for (100), and 2θ = 35.1° for (110) diffraction [75-78]. Almost no change in the spectra of model compounds can be detected in peak shapes or peak positions.

4. Conclusions

In this study, superhydrophobic hybrid paper sheets with varying inorganic particles and PDMS molecular weights in the coating formulation were prepared. All the samples (except the control sample prepared without filler incorporation) were nonwettable and possessed promising air and water barrier properties. Especially the hybrid sheets possessing only spherical fillers in the coating formulation revealed promising optical values with ΔE00 values below 1. The surface roughness values of these samples decreased with increasing PDMS molecular weight in the coating formulation, as revealed by Bendsten roughness analyses and confocal microscopy studies. However, the trend of decreasing ΔE_{00} values and roughnesses could not be detected for the samples possessing platelet-shaped particles. However, these hybrid paper sheets possessing platelet-shaped particles in the coating formulation revealed significantly lower air permeance values with respect to those of the control samples, as expected. All the samples had significant decreases above 90 % in Cobb values. FT-IR and XRD studies revealed the extent of chemical interactions and distribution behavior on the surface of the samples. Accordingly, it was concluded that the platelet-shaped particles are not present in exfoliated or intercalated form in the coating but are homogenously distributed on the paper substrates, as revealed by SEM studies. According to the FT-IR results, there is evidence of increased H-bonding and new covalent interactions, especially for hybrid paper sheets possessing only spherical particles in the coating formulation, but the extent of interactions in hybrid paper sheets with

platelet-shaped particles could not be well understood. Moreover, it was also revealed by SEM studies that the growing PDMS molecular weight in the coating formulation decreased the pore diameters of all the hybrid paper sheets. All in all, the studies done so far reveal that the method proposed for the preparation of the PDMS/GS/aero/N20 samples might be suitable for designing new packaging material alternatives.

Funding

This work was supported by TÜBİTAK 3501 National Young Researchers Career Development Program, Turkey. Project Number: 119M109.

Acknowledgments

Thanks to the support the of the TÜBİTAK 3501 National Young Researchers Career Development Programme, chemicals could be provided.

5. References

1. Bian P, Wang Y, Mc Carthy TJ. Rediscovering Silicones: The anomalous water permeability of "hydrophobic" PDMS suggests nanostructure and applications in water purification and anti-icing. Macromol Rapid Commun. 2021; 42: 2000682. https://doi.org/10.1002/marc.202000682.
2. Chen H, Wang B, Li J, Ying G, Chen F. High-strength and super-hydrophobic multilayered paper based on nano-silica coating and micro-fibrillated cellulose. Carbohyd Polym 2022; 288: 119371. https://doi.org/10.1016/j.carbpol.2022.119371.
3. Eduok U, Faye O, Szpunar J, Khaled M. Effect of silylating agents on the superhydrophobic and self-cleaning properties of siloxane/ polydimethylsiloxane nanocomposite coatings on cellulosic fabric filters for oil–water separation. RSC Adv 2021; 11: 9586-9599. https://doi.org/10.1039/D0RA10565A.
4. Ibrahim SA, Sultan MZ. Superhydrophobic coating polymer/silica nanocomposites: enhancing water vapor barrier properties of packaging paper with ultra-thin PS/silica nanocomposite polymer coating. Egypt J Chem. 2019; 62: 131-139. https://doi.org/10.21608/EJCHEM.2018.3842.1374.
5. Jia W, Kharraz JA, Choi PJ, Guo J, Deka BJ. An, A.K. Superhydrophobic membrane by hierarchically structured PDMS-POSS electrospray coating with cauliflower-shaped beads for enhanced MD performance. J Membr Sci. 2020; 597: 117638. https://doi.org/10.1016/j.memsci.2019.117638.
6. Lafraya A, Prieto C, Pardo-Figuerez M, Chiva A, Lagaron JM. Super-repellent paper coated with electrospun biopolymers and electrosprayed silica of interest in food packaging applications. Nanomaterials. 2021; 11: 3354. https://doi.org/10.3390/nano11123354.
7. Li H, He Y, Yang J, Wang X, Lan T, Peng L. Fabrication of food-safe superhydrophobic cellulose paper with improved moisture and air barrier properties. Carbohydr Polym. 2019; 211: 22-30. https://doi.org/10.1016/j.carbpol.2019.01.107.
8. Li X, Cao M, Shan H, Tezel FH, Li B. Facile and scalable fabrication of superhydrophobic and superoleophilic PDMS-co-PMHS coating on porous substrates for highly effective oil/water separation. Chem Eng J. 2019; 358: 1101-1113. https://doi.org/10.1016/j.cej.2018.10.097.
9. Li A, Wang G, Zhang Y, Zhang J, He W, Ren S, Xu Z, Wang J, Ma Y. Preparation methods and research progress of superhydrophobic paper. Coord Chem Rev. 2021; 449: 214207. https://doi.org/10.1016/j.ccr.2021.214207.
10. Mai Z, Shu X, Li G, Chen D, Liu M, Xu W, Zhang H. One-step fabrication of flexible, durable and fluorine-free superhydrophobic cotton fabrics for efficient oil/water separation. Cellulose 2019, 26: 6349-6363. https://doi.org/10.1007/s10570-019-02515-9.
11. Ni L, Zhu C, Zhang S, Cai P, Airoudj A, Vonna L, Hajjar-Garreau S, Chemto A. Light-induced crystallization-driven formation of hierarchically ordered superhydrophobic sol-gel coatings. Prog Org Coat. 2019; 135: 255-262. https://doi.org/10.1016/j.porgcoat.2019.05.045.
12. Abed RN, Kadhom M, Ahmed DS, Hadawey A, Yousif E. Enhancing Optical Properties of Modified PVC and Cr_2O_3 Nanocomposite. Trans Electr Electron Mater. 2021; 22: 317–327. https://doi.org/10.1007/s42341-020-00242-8.
13. Abed RN, Abed ARN, Yousif E. Carbon surfaces doped with (Co_3O_4-Cr_2O_3) nanocomposite for high-temperature photo thermal solar energy conversion via spectrally selective surfaces. Prog Color Colorants Coat. 2021; 14: 301-315. https://doi.org/10.30509/PCCC.2021.166749.1098.
14. Omer RM, Al-Tikrity ETB, Abed RN, Kadhom M, Jawad AH, Yousif E. Electrical conductivity and surface morphology of PVB films doped with different nanoparticles. Prog Color Colorants Coat. 2022; 15: 191-202. https://doi.org/10.30509 /pccc. 2021.166839.1120.
15. Abed RN, Abdallh M, Rashad AA, Hadawey A, Yousif E. New coating synthesis comprising CuO:NiO/C to obtain highly selective surface for enhancing solar energy absorption. J Polym Bull. 2021; 78: 433-455. https://doi.org/10.1007/s00289-020-03115-5.
16. Ruan X, Xu T, Chen D, Ruan Z, Hu H.

Superhydrophobic paper with mussel-inspired polydimethylsiloxane–silica nanoparticle coatings for effective oil/water separation. RSC Adv. 2020; 10: 8008-8015. https://doi.org/10.1039/c9ra08018j.
17. Teng Y, Wang Y, Shi B, Chen Y. Facile preparation of economical, eco-friendly superhydrophobic surface on paper substrate with excellent mechanical durability. Pro Org Coat. 2020; 105877. https://doi.org/10.1016/j.porgcoat.2020.105877
18. Barthwal S, Barthwal S., Singh B, Singh NB. Multifunctional and fluorine-free superhydrophobic composite coating based on PDMS modified MWCNTs/ZnO with self-cleaning, oil-water separation, and flame retardant properties. Colloids Surf, A 2020; 597: 124776. https://doi.org/10.1016/j.colsurfa.2020.124776
19. Teng Y, Wang Y, Shi B, Li X, Chen Y. Robust superhydrophobic surface fabrication by fluorine-free method on filter paper for oil/water separation. Polym Test 2020; 91: 106810. https://doi.org/10. 1016/j.polymertesting.2020.106810
20. Zhang J., Zhang L, Gong X. Large-scale spraying fabrication of robust fluorine-free superhydrophobic coatings based on dual-sized silica particles for effective antipollution and strong buoyancy. Langmuir. 2021; 37: 6042-6051. https://doi.org/10.1021/acs.langmuir.1c00706
21. Ma Y, He Q. Preparation of superhydrophobic conductive CNT/PDMS film on paper by foam spraying method. Colloids Surf A. 2022; 648: 129327. https://doi.org/10.1016/j.colsurfa.2022.129327
22. Li H, Luo Y., Yu, F. Peng, L. Simple and scalable preparation of robust and magnetic superhydrophobic papers by one-step spray-coating for efficient oil-water separation. Colloids Surf A. 2022; 640: 128449. https://doi.org/10.1016/j.colsurfa.2022.128449
23. Benselfeld T, Pettersson T, Wagberg L. Influence of surface charge density and morphology on the formation of polyelectrolyte multilayers on smooth charged cellulose surfaces. Langmuir. 2017,33(4): 968-979.https://doi.org/10.1021/acs.langmuir. 6b04217.
24. Heymann E, Rabinov G. The acid nature of cellulose. I equilibria between cellulose and salts. J Phy Chem. 1941; 45: 1152-1166. https://doi.org/10.1021/j150413a002.
25. Österberg M, Claesson PM. Interactions between cellulose surfaces: effect of solution pH. J Adhes Sci Technol. 2000; 14(5): 603-618. https://doi.org/10.1163/156856100742771.
26. Zhou Z, Ju X, Chen J, Wang R, Zhong Y, Li L. Charge-oriented strategies of tunable substrate affinity based on cellulase and biomass for improving in situ saccharification: A review. Bioresour Technol. 2021; 319: 12415. https://doi.org/10.1016/j.biortech.2020.124159.
27. Söz, C. Mechanical and wetting properties of coated paper sheets with varying 1 polydimethylsiloxane molecular masses in the coating formulation. Turk J Chem. 2022; 46: 283-294. https://doi.org/10.3906/kim-2104-57.
28. Kaya SS, Doğru D, Adeel S, Özomay M, Özomay Z. Environmentally friendly dyeing of waste cellulose fiberwith natural dye extract obtained from walnut shell (juglans regia), In: 4. International Cappadocia Scientific Research Congress, 2023, Nevşehir, Türkiye.
29. Doğru D, Kaya SS, Adeel S, Özomay M, Özomay Z. Mıcrowave-Assisted Dyeing Of Cotton Fabric Using Turkey Oak (Quercus Cerrıs L.) As A Source Of Natural Dye. In: 4. International Antalya Scientific Research And Innovative Congress, 2023, Turkey.
30. Hayta P, Oktav M, Ateş Ö, Özomay Z. Printability analysis of cyan color offset printing ink prepared with renewable materials. Anatolian J Forest Res 2022; 8(11): 111-115. https://doi.org/10.53516/ajfr.1204219.
31. Krumpfer JW, McCarthy TJ. Rediscovering silicones: "unreactive" silicones react with inorganic surfaces. Langmuir. 2011; 27: 11514-11519. https://doi.org/10.1021/la202583w.
32. Söz CK, Trosien S, Biealski M. Superhydrophobic hybrid paper sheets with janus type wettability. ACS Appl Mater Interfaces. 2018; 19(43): 37478-37488. https://doi.org/10.1021/acsami.8b12116.
33. Söz CK, Özomay Z, Ünal S, Uzun M, Sönmez S. Development of a nonwetting coating for packaging substrate surfaces using a novel and easy to implement method. Nord Pulp Pap Res J. 2021: 36(2): 331–342. https://doi.org/10.1515/npprj-2021-0017
34. Wacker Chemie Ag. HDK® N20 Pyrogenic Silica. [Internet] 2023 [cited 2023 Nov 22] Avaible from: https://www.wacker.com/h/en-us/pyrogenic-silica/ hdk-n20/p/000006084.
35. Sonmez S, Gong R, Fleming III PD, Wu Q, Pekarovicova P. The effects of the interaction of pigment coating with ink on the offset print quality. J Coat Technol. Res. 2022; 19(6): 1851-1858. https://doi.org/10.1007/s11998-022-00656-4.
36. Massadikova G, Özomay M, Özomay Z, Hasanova R. Analytical characterization of bible and textiles artifacts from sinope balatlar church excavations for conservation purposes. Med Archaeol Archaeom. 2022; 22: 3. https://doi.org/10.5281/zenodo.7268842
37. Yilgor I, Yilgor E, Kosak Söz, C. Superhydrophobic Polymer Surfaces: Preparation, Properties, and Applications, 1st ed. Engand: Smithers Rapra Technology; 2016.
38. Mboowa D, Chandra RP, Hu J, Saddler JN. Substrate Characteristics that influence the filter paper assay's ability to predict the hydrolytic potential of cellulase mixtures. ACS Sustain Chem Eng. 2020; 8(28): 10521-10528.https://doi.org/10.1021/acssuschemeng.0c02883.
39. Golizadeh M, Karimi A, Gandomi-Ravandi S, Vossoughib M, Khafajid M, Joghataei MT, Faghihi F. Evaluation of cellular attachment and proliferation on different surface charged functional cellulose

electrospun nanofibers. Carbohyd Polym. 2019; 207: 796-805.https://doi.org/10.1016/j.carbpol.2018. 12.028.
40. Lombardo S, Thielemans M. Thermodynamics of adsorption on nanocellulose surfaces. Cellulose. 2019; 26: 249-279. https://doi.org/10.1007/s10570-018-02239-2.
41. Isogai A. Cellulose nanofibers: recent progress and future prospects, J Fiber Sci Technol. 2020; 76(10): 310-326. https://doi.org/10.2115/fiberst.2020-0039.
42. Sönmez S, Sood S, Stoops M, Fleming III PD, Kecheng L, Wu Q, Salam A. Recycling of printed papers and usability in flexo printing packaging. Cellul Chem Technol. 2022; 56(7-8): 851-860. https://doi.org/10.35812/CelluloseChemTechnol.2022. 56.76.
43. Sonmez S, Arslan S. Investigation of the effects on ink colour of lacquer coating applied to the printed substrate in the electrophotographic printing system. Pol J Chem Technol. 2021; 23(2): 35-40. https://doi.org/10.2478/pjct-2021-0014.
44. Özomay M, Güngör F, Özomay Z. Determination of optimum dyeing recipe with different amount of mordants in handmade cotton fabrics woven with olive leaves by grey relational analysis method. J Text Inst. 2020; 113(6): 1048-1056. https://doi.org/10. 1080/00405000.2021.1908008.
45. Özomay Z, Şahin C, Keskin B. Investigation of the effect of different screening structures on print quality in digital printing system. Politeknik J. 2021; 24(3): 1213-1217. https://doi.org/10.2339/politeknik.884893.
46. Yilmaz, U.; Tutus, A.; Sonmez, S. Effects of using recycled paper in inkjet printing system on colour difference. Pigm Resin Technol. 2022; 51(3): 336-343. http://dx.doi.org/10.1108/PRT-03-2021-0032.
47. Aydemir C, Kasikovic N, Horwath C, Durdevic S. Effect of Paper Surface Properties on Ink Color Change, Print Gloss, and Light Fastness Resistance. Cellul Chem Technol. 2021; 55(1-2): 133-139. http://dx.doi.org/10.35812/CelluloseChemTechnol.20 21.55.14.
48. Kandi SG, Panahi B, Zoghi N. Impact of surface texture from fine to coarse on perceptual and instrumental gloss. Prog Org Coat. 2022; 107028. https://doi.org/10.1016/j.porgcoat.2022.107028.
49. Yong Q, Chang J, Liu Q, Jiang F, Wei D, Li H. Matt polyurethane coating: correlation of surface roughness on measurement length and gloss. Polymers. 2020; 12(326): 1-12. https://doi.org/10.3390/polym12020326.
50. Pino A, Pladellorens J, Colom FF, Cusola O, Tosas A. Using laser speckle to measure the roughness of paper. Tappi J. 2011; 10(3): 7-13. https://doi.org/ 10.1117/12.825072.
51. Khosravani A, Asadollahzade M, Rahmaninia M, Bahramifar N, Azadfallah M. The effect of internal application of organosilicon compounds on the hydrophobicity of recycled OCC paper. Bioresources. 2016; 11: 8257-8268. https://doi.org/10.15376/biores. 11. 4.8257-8268.
52. Fanta GF, Felker FC, Hay WT, Selling GW. Increased water resistance of paper treated with amylose-fatty ammonium salt inclusion complexes. Ind Crops Prod. 2017; 105: 231-237. https://doi.org/ 10.1016/j.indcrop.2017.04.060.
53. Rhim JW, Kim JH. Properties of poly(lactide)-coated paperboard for the use of 1-way paper. Cup J Food Sci. 2009, 74(2): 105-111. https://doi/10.1111/j.1750-3841.2009.01073.x.
54. Rumens CV, Ziai MA, Belsey KE, Batchelor JC, Holder SJ. Swelling of PDMS networks in solvent vapours; applications for passive RFID wireless sensors. J Mater Chem C. 2015; 3: 10091-10098. https://doi.org/10.1039/C5TC01927C.
55. Shen M, Liao X, Xianyu Y, Liu D, Ding T. Polydimethylsiloxane Membranes Incorporating Metal–Organic Frameworks for the Sustained Release of Antibacterial Agents. ACS Appl Mater Interfaces. 2022; 14(10): 12662-12673. https://doi.org/10.1021/ acsami.1c24921.
56. Mohammed Salih, S. Fourier Transform-Materials Analysis, 1st ed. In: IntechOpen, 2012, Rijeka, Croatia.
57. Garside P, Wyeth P. Identification of cellulosic fibres by FTIR spectroscopy - thread and single fibre analysis by attenuated total reflectance. Stud Conserv 2013; 48: 269-275. https://doi.org/10.1179/sic. 2003.48.4.269.
58. Yilgor E, Eynur T, Kosak C, Bilgin S, Yilgor I, Malay O, Menceloglu Y, Wilkes GL. Fumed silica filled poly(dimethylsiloxane-urea) segmented copolymers: preparation and properties. Polymer. 2011;52:4189-4198. https://doi.org/10.1016/j. polymer. 2011.07.041.
59. Rubio F, Rubio J, Oteo JL. A FT-IR study of the hydrolysis of tetraethylorthosilicate (TEOS). Spectrosc Lett 1998; 31(1): 199-219. https://doi.org/ 10.1080/00387019808006772.
60. Ly HQ, Taylor R, Day RJ, Heatley F. Conversion of polycarbosilane (PCS) to SiC-based ceramic Part 1. Characterisation of PCS and curing products. J Mater Sci. 2001; 13: 4037-4043. https://doi.org/10. 1023/A: 1017942826657.
61. Wang F, Chen P, Li X, Zhu B. Effect of colloidal silica on the hydration behavior of calcium aluminate. Chem Mater. 2018; 11: 1849. https://doi.org/10. 3390/ma11101849.
62. Ilić I, Jović-Jovičić N, Banković P, Mojović Z, Lončarević D.I., Gržetić, Milutinović-Nikolić, A. Adsorption of nicotine from aqueous solutions on montmorillonite and acid–modified montmorillonite. Sci Sintering. 2019; 51: 93-100. https://doi.org/10. 2298/SOS1901093I.
63. Kim E, Kim S, Kim SS. Preparation and characterization of monodisperse polystyrene-silica nanocomposites. Macromol Res 2015; 23(8): 787-794. https://doi.org/10.1007/s13233-015-3097-y.
64. Spence A, Kelleher BP. FT-IR spectroscopic analysis of kaolinite–microbial interactions. Vib Spectrosc 2012; 61: 151-155. https://doi.org/10.1016/j. vibspec. 2012.02.019.

65. Djomgoue P, Njopwouo D. FT-IR Spectroscopy Applied for Surface Clays Characterization. J Surf Eng Mater Adv Technol. 2013; 3: 275-282. http://dx.doi.org/10.4236/jsemat.2013.34037.
66. Chen M, Chen X, Zhang C, Cui B, Li Z, Zhao D, Wang Z. Kaolin-enhanced superabsorbent composites: synthesis, characterization and swelling behaviors. Polymers. 2021; 13: 1204. https://doi.org/10.3390/polym13081204.
67. Meng Y, Wang S, Guob Z, Cheng M, Li J, Li D. Design and preparation of quaternized pectin-Montmorillonite hybrid film for sustained drug release. Int J Biol Macromol. 2020; 154: 413-420. https://doi.org/10.1016/j.ijbiomac.2020.03.140.
68. Dlaminia DS, Lia J, Mamba MM. Critical review of montmorillonite/polymer mixed-matrix filtration membranes: Possibilities and challenges. Appl Clay Sci. 2018; 168: 21-30. https://doi.org/10.1016/ j.clay.2018.10.016.
69. Huang MY, Chen Y, Yan X, Guo XJ, Dong L, Lang WZ. Two-dimensional Montmorillonite membranes with efficient water filtration. J Membr Sci. 2020; 624: 118540. https://doi.org/10.1016/j. clay.2018.10.016.
70. Wang Y, Li Z, Wu C, Zhou P, Zhou J, Huo J, Davis K, Konstantinou A, Nguyen H, Cao Y. Polyamideimide dielectric with montmorillonite nanosheets coating for high-temperature energy storage. Chem Eng J. 2022; 437: 135430. https://doi.org/10.1016/j.cej.2022.135430.
71. Adeniyi AG, Abdulkareem SA, Emenike EC, Abdulkareem MT, Iwuozor KO, Amoloye MA, Ahmed II, Awokunle OE. Development and characterization of microstructural and mechanical properties of hybrid polystyrene composites filled with kaolin and expanded polyethylene powder. Results Eng. 2022; 14: 100423. https://doi.org/10.1016/j.rineng.2022.100423.
72. Vijayaraghavan J, Jeevakkumar R, Venkatesan G, Rengasamy M, Thivya, J. Influence of kaolin and dolomite as filler on bond strength of polyurethane coated reinforcement concrete. Constr Build Mater. 2022; 325: 126675. https://doi.org/10.1016/j.conbuildmat. 2022.126675
73. Barthlott W, Neinhuis C. Purity of the sacred Lotus, or escape from contamination in biological surfaces. Planta. 1997; 202: 1-8. https://doi.org/10. 1007/s004250050096.
74. Cheng H, Yang J, Liu Q, Zhang J, Frost R L. A spectroscopic comparison of selected Chinese kaolinite, coal bearing kaolinite and halloysite-A mid-infrared and near-infrared study. Spectrochim. Acta, Part A. 2010; 77:856-861. https://doi.org/10.1016/j.saa.2010.08.018.
75. Kakali G, Perraki T, Tsivilis S, Badogiannis E. Thermal treatment of kaolin: the effect of mineralogy on the pozzolanic activity. Appl Clay Sci. 2001; 20: 73-80. https://doi.org/10.1016/S0169-1317(01)00040-0.
76. Villa RVV, Frías M, Rojas MIS, Vegas I, García R. Mineralogical and morphological changes of calcined paper sludge at different temperatures and retention in furnace. Appl Clay Sci. 2007; 36: 2279-286. https://doi.org/10.1016/j.clay.2006.10.001.
77. Kumar AH, Ahamed MB, Deshmukh K, Sirajuddeen MS. Morphology, dielectric and EMI shielding characteristics of graphene nanoplatelets, montmorillonite nanoclay and titanium dioxide nanoparticles reinforced polyvinylidenefluoride nanocomposites. J Inorg Organomet Polym Mater 2021; 31: 2003-2016. https://doi.org/10.1007/s10904-020-01869-z.
78. Wilson J, Cressey G, Cressey B, Cuadros J, Ragnarsdottir KV, Savage D, Shibata M. The effect of iron on montmorillonite stability. (II) Experimental investigation. Geochim Cosmochim Acta. 2006; 70: 323-336. https://doi.org/10.1016/j.gca.2005.09.023.

How to cite this article:
Evren G, Koşak Söz Ç, Özomay Z, Uzun M, Sönmez S. Effect of the Coating Formulation on the Barrier Properties and Final Appearance of Non-wettable Hybrid Paper Sheets. Prog Color Colorants Coat. 2024;17(3):239-262. https://doi.org/ 10.30509/pccc.2024.167221.1257.